

# The qualities of dyed YAG:Ce<sup>3+</sup>@SiO<sub>2</sub> for WLEDs via energy conversion

Phung Ton That<sup>1</sup>, Phan Xuan Le<sup>2</sup>

<sup>1</sup>Faculty of Electronics Technology, Industrial University of Ho Chi Minh City, Ho Chi Minh City, Vietnam

<sup>2</sup>Faculty of Mechanical-Electrical and Computer Engineering, School of Engineering and Technology, Van Lang University, Ho Chi Minh City, Vietnam

## Article Info

### Article history:

Received Jun 9, 2021

Revised May 31, 2022

Accepted Jul 8, 2022

### Keywords:

Correlated color temperature

Mie-scattering theory

Phosphor structure

SiO<sub>2</sub> nano-particles

## ABSTRACT

Y<sub>3</sub>Al<sub>5</sub>O<sub>12</sub>:Ce<sup>3+</sup> (YAG:Ce<sup>3+</sup>), the most common yellow phosphor for WLEDs, has a red insufficiency in its light spectrum. The Ce<sup>3+</sup> spectral profile is modified in this research using surface-located ATTO-Rho101 dye molecules, which have powerful, wide impregnation in the greenish-yellow spectroscopic zone of Ce<sup>3+</sup> radiation and vivid red-emitting radiation. To create a spherical shell and evenly dispersed micro and nanometer YAG:Ce<sup>3+</sup>, a modified solvothermal technique is applied. Surface SiO<sub>2</sub> covering and synchronized dye embedding are accomplished using solvothermally generated YAG:Ce<sup>3+</sup>, temperature-stimulated micro-YAG:Ce<sup>3+</sup>, plus commercialized phosphorus. Upon blue light excitation, the accumulated YAG:Ce<sup>3+</sup>@SiO<sub>2</sub>+dye powder exhibits efficient radiative conversion/reintake from Ce<sup>3+</sup> within the internal structure of YAG to the pigment particles from the SiO<sub>2</sub> external shell, despite the phosphors' diameter; which likely boosts its red radiation. Fluorescence microscopy would be a suitable way to determine the reabsorption of powdered substances.

This is an open access article under the [CC BY-SA](https://creativecommons.org/licenses/by-sa/4.0/) license.



## Corresponding Author:

Phan Xuan Le

Faculty of Mechanical-Electrical and Computer Engineering, School of Engineering and Technology

Van Lang University

Ho Chi Minh City, Vietnam

Email: le.px@vlu.edu.vn

## 1. INTRODUCTION

The invention of powerful blue-colored light-emitted diodes (LEDs) during the 1990s marked a revolutionary era of solid-state illuminating [1], [2]. Luminescent efficiency, excellent color rendering indices (CRI), and a variety of other enhanced qualities have been developed in this general lighting industry in previous decades [3], [4]. Besides the popularly used LED lights that are mostly relied on phosphorus-converting LEDs (pc-LEDs) because of convenience, dependability, and low cost of production, white-colored light-emitted diodes (WLEDs) are created by fusing blue, green, and red LED chips [5]. The original commercially available WLEDs were made from fusing a yellowish-emitted garnet phosphorus, Y<sub>3</sub>Al<sub>5</sub>O<sub>12</sub>:Ce<sup>3+</sup> (YAG:Ce<sup>3+</sup>), featuring a blue-emitted-LED chip. This method is still the most common way to make WLEDs, and Ce<sup>3+</sup>-doped gems (plus configurational adjustments) are still the most widely used yellow phosphors in pc-LEDs. For example, throughout the 1960s, YAG:Ce<sup>3+</sup>, a material with a strong quantum yielding (QY)>85% despite being heated at 200 °C, was first characterized for fundamental utilization in cathode ray tubes or CRTs [6]-[8]. Through the equivalence, the stimulator Ce<sup>3+</sup> absorbed blue-emitted LED output in this phosphor and spin-permitted 4f 1 → 5d1 interconstructional shift as well as generated yellow-emitted light through the opposite 5d1 → 4f 1 (2F5/2 and 2F7/2 spin-track dividing rates) shift resulting in an

expansive emitting spectrum featuring a full width at a half-maximum (FWHM) of over 100 nm. The spectral pattern of this emission was red-deficient; as a result, pc-LEDs packed beside YAG:Ce<sup>3+</sup> only emitted mild and blue-white tone lighting emission comprising strong correlating hue heats correlated color temperature (CCT>4500) and moderate CRI figures (Ra<75), failing to keep up with the growing demand for rising quality mild white-emitted household lighting for colorful presentations and public safety [9]-[12].

One of the easiest methods to improve low color rendering, caused by a lack of the red element in the lighting spectrum content as using YAG:Ce<sup>3+</sup> for mild tone WLEDs, is to include a red-emitted phosphorus forward the blue-emitted LED phosphorus mixture. Because of the various measurements and exterior properties of each phosphorus, agglomeration or sedimentation emerges easily in this multi-phosphor system. Furthermore, color dispersion of WLEDs will occur because of retaking procedures and varying phosphorus deterioration levels. But a mono-element phosphorus featuring many emitting centers or red-shifting rays is seen to be a good method for enhancing the efficiency of WLEDs. Codoping red-disputed lanthanide stimulators as Pr<sup>3+</sup> (611 nm, <sup>1</sup>D<sub>2</sub> → <sup>3</sup>H<sub>4</sub>), Sm<sup>3+</sup> (616 nm, <sup>4</sup>G<sub>5/2</sub> → <sup>6</sup>H<sub>7/2</sub>) and Eu<sup>3+</sup> (590 and nm, <sup>5</sup>D<sub>0</sub> → <sup>7</sup>F<sub>1,2</sub>) or shifting of metallic particles like Cr<sup>3+</sup> (685 nm, <sup>2</sup>E → <sup>4</sup>A<sub>2</sub>)<sup>10</sup> and Mn<sup>2+</sup> (594 nm, <sup>4</sup>T<sub>1</sub>(<sup>4</sup>G) → <sup>6</sup>A<sub>1</sub>(<sup>6</sup>S)) via Mn<sup>2+</sup>-Si<sup>4+</sup> co-replacement for Y<sup>3+</sup>-Al<sup>3+</sup>(tetrahedral) was demonstrated to offer further red emissions within YAG:Ce<sup>3+</sup> [13], [14]. However, because of the low assimilation of particles from the blue-emitted spectral region or ineffective energy conversion by Ce<sup>3+</sup>, the amplification of the red component is highly restricted in most of these circumstances. Another way to red-displacement Ce<sup>3+</sup> 5d<sup>1</sup> → 4f<sup>1</sup> output is to change surrounding region of the Ce<sup>3+</sup> dischargers by substituting La<sup>3+</sup> or Gd<sup>3+</sup> for Y<sup>3+</sup>, Gd<sup>3+</sup>-Ga<sup>3+</sup> co-replacement for Y<sup>3+</sup>-Al<sup>3+</sup>(tetrahedral), or Mg<sup>2+</sup>-Si<sup>4+</sup> co-replacement for Al<sup>3+</sup> (octahedral) – Al<sup>3+</sup> (tetrahedral). Such red-displacement is frequently attained depending on the efficiency, particularly at elevated heats. A third method is to investigate Ce<sup>3+</sup>-doped silica almandine exhibiting output peaks of 505-605 nm with more elevated ambient temperature QYs as compared to YAG:Ce<sup>3+</sup> phosphors. Furthermore, because the Ce<sup>3+</sup> ions are coordinated with N<sub>3</sub>, substituting Al<sup>3+</sup> (tetrahedral)-O<sup>2-</sup> with Si<sup>4+</sup>-N<sup>3-</sup> results in an additional red portion (620–630 nm) in the emitted bands. Instead, we suggest a new technique in this study to adjust the Ce<sup>3+</sup> spectroscopic property in a YAG mono-element phosphorus for red-emitted element amplification [15], [16]. To transform the excess greenish-yellow spectroscopic property into a red one by power conversion, organic dye molecules were used instead of metal ions. Organic dyes and derivatives were made to cater to a variety of uses, encompassing conventional textile and emulsified coloring, modern astronomical cells as well as physiological detectors, and high-tech optoelectronic devices [17], [18]. As a result, there are several options for determining the acceptable pigments containing strong absorbance throughout the greenish-yellow spectroscopic range suiting the YAG:Ce<sup>3+</sup> emission. Despite strong molar absorption indices, broad emitting spectrum, strong fluorescence QY, and minor Stokes changes caused by the poor vibrational release and inner conversion, these organic particles appear to be more photo-bleached than inorganic species during heating and irradiation. When dye molecules are integrated into the firm substrates (for example, silicon ions, translucent polymers, epoxy coatings), the “isolating impact” from atmospheric gas and the constrained motion of the coloring particles greatly reduce heating and photo-oxidation and inhibit photobleaching; as a result, they are advantageous for WLED uses. Different natural fluorescent dyes have already been investigated to use for WLEDs.

## 2. METHOD

### 2.1. Micro-YAG:Ce<sup>3+</sup>@SiO<sub>2</sub> + pigment production, nano-YAG:Ce<sup>3+</sup>@SiO<sub>2</sub> + pigment formulation, and commercialized YAG:Ce<sup>3+</sup>/(SiO<sub>2</sub> + dye) composition

A version of the well-known *Stöber* process was used to coat the surface with SiO<sub>2</sub> and simultaneously incorporate Rho101-APTS compounds as the exterior's dye. Under continuous stirring and ultrasonication, sufficient volumes namely 0.1 g of YAG:Ce<sup>3+</sup> or 0.01 g of nano-YAG:Ce<sup>3+</sup> in 30 mL of ethanol solvent, proceeded by the insertion of ammonium fluid (3.2 mL, 16 percent). After that, moderate volume in the ethanol Rho101-APTS conjugates solvent was included in the mixture and stirred for half an hour. After that, add tetra-ethyl orthosilicate (TEOS) 0.05 mL and mix for another 12 hours. The silica covering and dye dipping were created by dehydration and vaporization in the TEOS as well as silane molecules in the compounds using an ammonium solvent reagent. The resultant mixture was separated after the reaction to obtain the silicate-covered nanocomposition using pure ethanol, referring as micro-YAG:Ce<sup>3+</sup>@SiO<sub>2</sub> + dye and nano-YAG:Ce<sup>3+</sup>@SiO<sub>2</sub> + dye, accordingly. Using a calibration curve, the filters were accomplished absorbance analyses estimating remnant Rho101-APTS's level. The dyes in the shells were quantified via deducting any remaining pigment in the filters in the initial edition. This coating method was repeated with the aim of improving the pigment's volume outside YAG:Ce<sup>3+</sup> cover which yields micro- YAG:Ce<sup>3+</sup>/(SiO<sub>2</sub> + dye) samples [19], [20].

Due to huge measurement, small surface-to-amount proportion, with flat texture, commercial YAG:Ce<sup>3+</sup> shows poor suspension characteristics. Polyvinylpyrrolidone (PVP) was used to pre-adjust 1.2 g of

phosphors by continuous mixing in a PVP 0.3 mm ethanol extract mixture, followed by extensive rinsing before surface SiO<sub>2</sub> adjustment and dye incorporation. A moderate SiO<sub>2</sub> portion was applied to the flattened top layer whenever the same method described above is used; thus, the surface treatments were performed five times to store enough amounts of dye into the SiO<sub>2</sub> layer. Many divided SiO<sub>2</sub> nanoparticles developed in the solution in this situation. To eliminate the SiO<sub>2</sub> nano-ions within the supernatant solvent, a limited-pace mixing of 1000 rpm and numerous sessions of decantation were used. Commercial YAG:Ce<sup>3+</sup>@(SiO<sub>2</sub>+dye) was the name given to the final products.

## 2.2. Scattering computation

The scattered parameter  $\mu_{sca}(\lambda)$ , anisotropic component  $g(\lambda)$ , along with declined diffused parameter  $\delta_{sca}(\lambda)$  could be calculated using Mie-scattering theory [21]-[25] via the formulas:

$$\mu_{sca}(\lambda) = \int N(r)C_{sca}(\lambda, r)dr \quad (1)$$

$$g(\lambda) = 2\pi \int_{-1}^1 p(\theta, \lambda, r)f(r)\cos\theta d\cos\theta dr \quad (2)$$

$$\delta_{sca} = \mu_{sca}(1 - g) \quad (3)$$

where  $N(r)$  represents the diffusive particle dispersion concretion (mm<sup>3</sup>),  $C_{sca}$  represents the scattered cross-sections (mm<sup>2</sup>). The phase function is shown by  $p(\theta, \lambda, r)$ ,  $\lambda$  denotes the illumination wavelength with measure unit in nm,  $r$  illustrates the diffusional particle range (m),  $\theta$  signifies the scattered angular unit (°C),  $f(r)$  denotes diffusor measurement dispersion function in the phosphorus coating:

$$f(r) = f_{dif}(r) + f_{phos}(r) \quad (4)$$

$$N(r) = N_{dif} + N_{phos}(r) = K_N \cdot [f_{dif}(r) + f_{phos}(r)] \quad (5)$$

$N(r)$  is composed of the diffusional component population  $N_{dif}(r)$  plus the phosphorus molecule volume  $N_{phos}(r)$ . The size dispersion functioning statistic of the distributor and phosphorus ion is  $f_{dif}(r)$  and  $f_{phos}(r)$ . The number of diffusor units ( $K_N$ ) in each distributor ratio is estimated as shown in:

$$c = K_N \int M(r)dr \quad (6)$$

In which  $M(r)$  is the bulk dispersion in the diffusional session, as specified by the following expression:

$$M(r) = \frac{4}{3}\pi r^3 [\rho_{dif}f_{dif}(r) + \rho_{phos}f_{phos}(r)] \quad (7)$$

The diffuser and phosphor crystal densities are  $\rho_{dif}(r)$  and  $\rho_{phos}(r)$ , respectively. The following expression will calculate  $C_{sca}$  in Mie theory:

$$C_{sca} = \frac{2\pi}{k^2} \sum_{n=0}^{\infty} (2n+1)(|a_n|^2 + |b_n|^2) \quad (8)$$

In which  $k = 2\pi/\lambda$ , whereas  $a_n$  and  $b_n$  can be computed in the following equations:

$$a_n(x, m) = \frac{\psi'_n(mx)\psi_n(x) - m\psi_n(mx)\psi'_n(x)}{\psi'_n(mx)\xi_n(x) - m\psi_n(mx)\xi'_n(x)} \quad (9)$$

$$b_n(x, m) = \frac{m\psi'_n(mx)\psi_n(x) - \psi_n(mx)\psi'_n(x)}{m\psi'_n(mx)\xi_n(x) - \psi_n(mx)\xi'_n(x)} \quad (10)$$

The refractive index is illustrated as  $x, m$  in which  $x = k.r$ ; besides,  $\psi_n(x)$  and  $\xi_n(x)$  are the Riccati - Bessel roles. As a result, the silicon's proportional refraction indexes of the distributor ( $m_{dif}$ ) and phosphorus

( $m_{phos}$ ) are respectively measured as  $m_{dif} = n_{dif}/n_{sil}$  and  $m_{phos} = n_{phos}/n_{sil}$  and followed by the expression of the phase function [26]-[28]:

$$p(\theta, \lambda, r) = \frac{4\pi\beta(\theta, \lambda, r)}{k^2 C_{sca}(\lambda, r)} \quad (11)$$

The following expression represents the angular scattering amplitudes  $\beta(\theta, \lambda, r)$ ,  $S_1(\theta)$  and  $S_2(\theta)$ .

$$\beta(\theta, \lambda, r) = \frac{1}{2} [|S_1(\theta)|^2 + |S_2(\theta)|^2] \quad (12)$$

$$s_1 = \sum_{n=1}^{\infty} \frac{2n+1}{n(n+1)} [a_n(x, m)\pi_n(\cos\theta) + b_n(x, m)\tau_n(\cos\theta)] \quad (13)$$

$$s_2 = \sum_{n=1}^{\infty} \frac{2n+1}{n(n+1)} [a_n(x, m)\tau_n(\cos\theta) + b_n(x, m)\pi_n(\cos\theta)] \quad (14)$$

We employed a two-stage solvothermal procedure for the task of generating micro-YAG:Ce<sup>3+</sup>@YAG with nano-YAG:Ce<sup>3+</sup> as controls. The observation from SEM and TEM showed that many YAG nanoparticles with a diameter of fewer than 100 nanometers can be detected from YAG:Ce<sup>3+</sup> microparticles' surfaces. The pre-dispersed YAG:Ce<sup>3+</sup> generated numerous exposed crystal facets during the second solvothermal stage, which acted as favorable germination locations for a secondary expansion because of the reduced activated energy. Germination is more likely to occur at these favored places. The YAG:Ce<sup>3+</sup> microspheres, as previously stated, principally obtained have uneven surface areas with poly-crystalline; thus, the exterior-disclosed aspects are made up of parts divided by grainy barriers. Consequently, several individual nanocrystals developed on the microspheres instead of a contiguous mono-crystalline cover. There were, however, instances of homogeneous nucleation. Also from monitoring the SEM and TEM images, the supernatant generated by limited germination from the products generated upon the 2nd hydrothermal method reaction contained numerous relatively small YAG:Ce<sup>3+</sup> nanocrystals (nano-YAG:Ce<sup>3+</sup> once employing Ce<sup>3+</sup>-doped YAG crystallize precursor chemicals) ranging in size from 5 to 15 nm. On nano-YAG:Ce<sup>3+</sup>, clear lattice fringes were seen, confirming single crystallinity. The second reaction process was also affected by the self-assembly process. Several sphere-shaped aggregates possessing diameters between 50 and 200 nm can also be seen. On nano-YAG:Ce<sup>3+</sup>, silicate top-layer covering and pigment enrooting were carried out using similar methods.

As shown in Figure 1, surface coating and pigment incorporation were subsequently performed on micro specimens following calcination and also commercialized phosphorus coating for red-pigmented output amplification. Because of their bigger sizes and flat surface, SiO<sub>2</sub> grew slower and more difficult on commercialized phosphors' outer layer. It took five cycles to find sufficient concentrations of SiO<sub>2</sub> and dye molecules. Chemical changes caused uneven exterior using inadequate and/or sparse SiO<sub>2</sub> sheets, as seen in Figure 2. After repeating the covering procedure with more than five cycles, it was discovered that SiO<sub>2</sub>'s exterior layer and the number of pigment varieties did not rise sequentially.

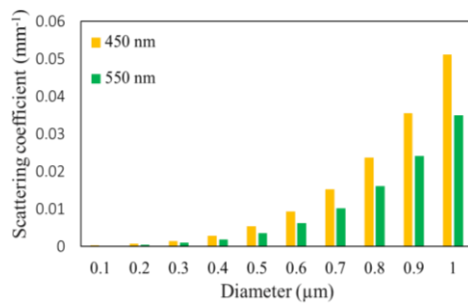


Figure 1. SiO<sub>2</sub> scattered coefficients at 450 as well as 550 nm

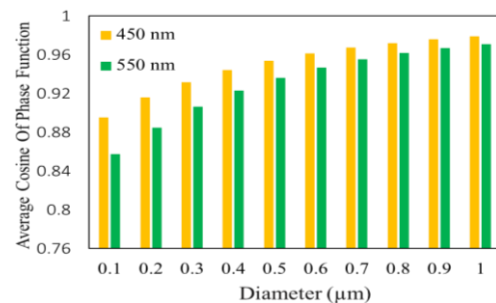


Figure 2. SiO<sub>2</sub> phase functioning at 450 as well as 550 nm

### 3. RESULT AND DISCUSSION

A certain amount of the maximum CCT is reduced to the minimum CCT to compute the angular-dependent CCT uniformity. As shown in Figure 3 the results of the analyses of different weights of  $\text{SiO}_2$  nano-particles to maximize CCT deviation. The stimulation bands for  $\text{Ce}^{3+}$  often comprise two discrete peaks at 330, 450 nm owing to electron-based transitioning among the  $\text{Ce}^{3+}$  baseline phase and the various crystalline sector-breaking elements of the exciting 5d phase of  $\text{Ce}^{3+}$  ( $^2\text{F}_{5/2,7/2} \rightarrow 5\text{d}^1$  transitions)<sup>2</sup>. This is true for the heat-treated micro-YAG: $\text{Ce}^{3+}$  sample, as seen in Figure 3 a considerable distance among two exciting regions. Nevertheless, both bands in two immaculate samples appear significantly extended and merged. As a result, a constant large range with a wavelength measured at 300 to 500 nm was obtained. The heat-treated micro-YAG: $\text{Ce}^{3+}$  spectra had virtually little functional stimulation at 390 nm. While that of micro-YAG: $\text{Ce}^{3+}$  is higher, it was roughly equivalent to the blue band at around 450 nm. The novel region remained detectable inside the spectra of nano-YAG: $\text{Ce}^{3+}$ , but at a reduced comparative amplitude. Additionally, the two immaculate samples' spectrum showed blue shifts, with the shift being higher for nano-YAG: $\text{Ce}^{3+}$ . Due to the 4f configuration of the  $\text{Ce}^{3+}$  ion, on ultraviolet (UV) or blue photon irradiation, only a particle would be advocated into a 5d orbital, which left the 4f shell unoccupied; however, because the 4f particles are effectively insulated from its borderings by the sealed 5s and 5p electronic configuration, the particles inhabiting the 5d orbital are further susceptible compared to spectroscopic probes to adjustments in the regional symmetry. The direct breaking data for the 5d orbital within the crystal field may thus be seen in the  $\text{Ce}^{3+}$  excitation spectrum. Because of the particles' modest diameters with sophisticated micro configurations, just one single D2 site asymmetry for  $\text{Ce}^{3+}$  particles is present in the YAG: $\text{Ce}^{3+}$  substrate lattice; thus, the widening and blue-colored transitions are directly related to surface/interface impacts. Carbonization of micro-YAG: $\text{Ce}^{3+}$  hardly influenced the total diameter yet rapidly stopped the spreading activities because of its large diameter of particles and restricted Brunauer-Emmett-Teller (BET) exterior surface. As a result, instead of surface impacts, the new spectrum responses should be attributed to interface impacts. When the smaller nano units were absorbed into the microspheres, they created a significant number of interfaces.

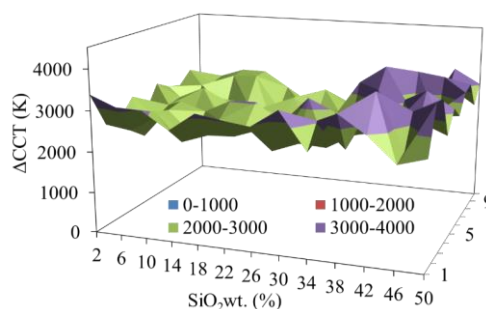


Figure 3. CCT deviations of  $\text{SiO}_2$  particles with different diameters

Regional asymmetry ought to be loosened as well as distinct to that of the protons within the granules. The moderately deformed/disorganized surrounding setting for  $\text{Ce}^{3+}$  at the interfaces was thought to reduce crystallized region intensity, resulting in the less straightforward breaking for the 5d orbital and higher electronic power rates of the 5d particles; thus, exciting relocations from the baseline phase to the 5d1 stimulated condition compelled higher power, which evidenced by the blue-pigmented changes of the exciting region and the emergence of the novel reflectance spectra upon the increased power aspect within  $\text{Ce}^{3+}$  regions in the grains. The novel range around 390 nm undoubtedly is attributable to exterior influences due to nano-YAG: $\text{Ce}^{3+}$  smaller size and bigger surface area; nonetheless, no further spectroscopic reactions or further evident blue deviations were seen in comparison with micro-YAG: $\text{Ce}^{3+}$ . As a result, surface and interface effects had different effects on the PL: interfacing influences encouraged the innovative stimulation range development, whereas surface impacts promoted the spectroscopic blue deviations. Surface featured more mechanical properties (for instance fractured and hanging linkages) and exterior-adsorbing forms because of the wider surfacing region, with greater surfaced pressure caused by its insignificant magnitude, appear to distort the surrounding environment of the  $\text{Ce}^{3+}$  surface and inner activators adjusting the crystalline sheet, and hence the exciting progress a different way. These changes may reduce direct breaking in the 5d orbital while increasing 5d electronic outputs of energy, as per researchers. There is a rising demand for higher energy from the stimulation shifts among the floor phase and the 5d1 exciting phase, as well as opposite emitted changes. As a result, additionally, noticeable blue-emitted transitions were seen in either the blue excitement region as shown in Figure 4 or the yellowish-green emitted region of nano-YAG: $\text{Ce}^{3+}$ .

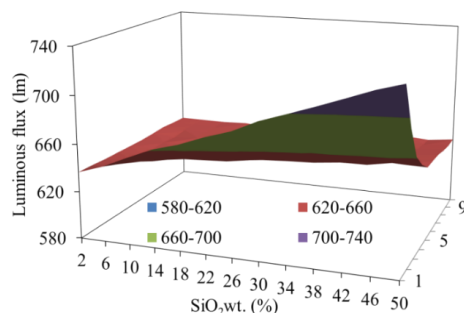


Figure 4. Various measurements in the SiO<sub>2</sub> ions luminous fluxes

Because of the ion transfer process from the minimum crystalline breaking element in the 5d phase to the base phase Ce<sup>3+</sup> (<sup>2</sup>F<sub>5/2</sub>, <sup>2</sup>F<sub>7/2</sub>) in the YAG host matrix, a standard broadband of Ce<sup>3+</sup> was detected in the emission spectra of as shown in Figure 5, ranging between 475 and 650 nm which reaches its peak at 550 nm. The stimulation towards the 455 nm blue-color region and the new 390 nm region in the illuminating beam of micro or nano-YAG:Ce<sup>3+</sup> was blue-diverse moderately against the illumination of micro-YAG:Ce<sup>3+</sup> post calcination process due to Ce<sup>3+</sup> surface and/or interfacial impacts. Because both excitations predominantly relate to various Ce<sup>3+</sup> units in the surfaces/interfaces as well as the interior particles, the blue shift for the excitation under 390 nm within a given sample is larger than for the excitation at 455. The more loosened crystalline fields influence in the surfaces/interfaces versus in the interior particles lead to a lower power breaking of the 5d particle in agitated Ce<sup>3+</sup>, resulting in a greater energy gap on 390 nm excitation across the low-reclining 5d<sup>1</sup> exciting phase towards the baseline stage. Under stimulation at 450 nm, micro-YAG:Ce<sup>3+</sup> emitted a brilliant yellow-emitted output as shown in Figure 6 featuring an 18.1% outward QY. Given the comparable superiority reduced potential of the Ce<sup>4+</sup>/Ce<sup>3+</sup> (1.44 V) pair, seemingly Ce<sup>4+</sup> particles were rapidly decreased in place of Ce<sup>3+</sup> using ethylenediamine (EDA) agents throughout the solvothermal synthesis. EDA and oleylamine have earlier been shown to reduce Eu<sup>3+</sup> → Eu<sup>2+</sup> during thermolysis and solvothermal reactions. The outward QY after calcination was 18.2 percent.

In the range of blue-color spectrum band (400-500 nm), the dye displays almost no effective excitation. Conversely, the standard wide region (300-500 nm) after Ce<sup>3+</sup> excitation was easily noticed by observing the dye's 615 nm red emission, besides the  $\pi \rightarrow \pi^*$  ion stimulation of a soluble carbon-carbon dual connection as in pigment particle (270 in UV, 550 in green, and 587 in yellow bands, measured in nm) which proves the effective energy conversion of the Ce to the pigment. Furthermore, dual circuits of surface treatments generated nearly twice stronger direct excitation in the dyes' region (500-600 nm), and just a very minor increment within the implicit stimulation area of Ce<sup>3+</sup> particles. Such a thing means that just a small portion of the dye molecules was involved in the energy conversion. When the surface-treated samples were excited into the blue band of Ce<sup>3+</sup>, greater red emissions (at 615 nm) matching the dyed areas were found within emission spectra. The dye emissions occurred and were amplified at the expenditure of greenish-yellow Ce<sup>3+</sup> emitted output that increased the red-emitted portions in the entire spectra, favoring the mild WLEDs, due to the characteristics of the energy conversion. If the top layer treatment process was duplicated, the intensity only increased marginally.

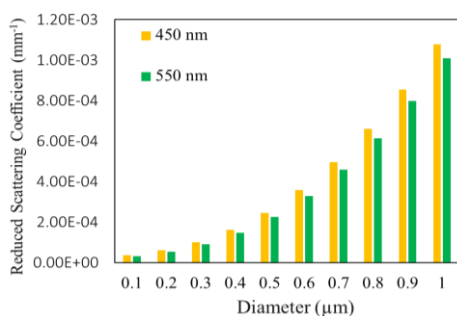


Figure 5. Decreased scattering coefficients of SiO<sub>2</sub> granules of diverse diameters and wavelengths in the range of 450-550 nm

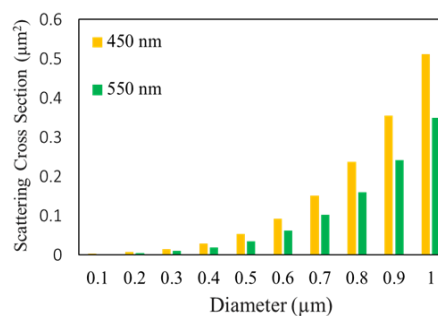


Figure 6. The scattered crossed-section in SiO<sub>2</sub> granules of diverse diameters and wavelengths in the range of 450-550 nm

#### 4. CONCLUSION

Finally, using a customized solvothermal approach, spherical-structured and strongly diffused micro- YAG:Ce<sup>3+</sup> phosphors as well as nano-YAG:Ce<sup>3+</sup> nano-crystalline particles are produced, and also SiO<sub>2</sub>'s outer layer covering and integrated to ATTO-Rho101 colorants (such as commercialized YAG:Ce<sup>3+</sup> phosphorus) to improve the red-color spectrum element within YAG:Ce<sup>3+</sup> yellow-emitted phosphors on mild WLEDs application. To generate brilliant PL, EDA was used in the form of a solvent as well as a reduction reaction. The samples were analyzed and described in detail, including their sizes, geometries, crystalline structure, components, and luminescence properties. The protonated amine type' exterior covering was removed after heat treatment on micro- YAG:Ce<sup>3+</sup>, and PL comparisons were made. Because of the loosened regional symmetries on either interface or surfaces, the excitation spectra of Ce<sup>3+</sup> dramatically widened and linked, providing a consistently wide range extending around 300 and 500 nm. Ce<sup>3+</sup> PL was affected differently by interface and surface impacts. Within the micro- YAG: Ce<sup>3+</sup>, interface effects moved the stimulation, as well as PL regions yet, had no effect on Ce<sup>3+</sup> dynamics; in nano-YAG: Ce<sup>3+</sup>, surface effects impacted both. The illumination in micro-YAG:Ce<sup>3+</sup> showed inadequate photograph-heating consistency when surfacing treatment with SiO<sub>2</sub> or YAG or integration into an epoxy resin matrix procedures are proceeded owing to Ce<sup>3+</sup> → Ce<sup>4+</sup> oxidative degradation by protonated amine species on the substrates on such stimulation by combustion or photoirradiation instead of gaseous Oxy sources from the surrounding environment. The PL of micro-YAG: Ce<sup>3+</sup> was found to be suppressed more effectively by stimulating irradiation. The material's photograph-thermal consistency was considerably improved by high calcination temperatures.

#### ACKNOWLEDGEMENTS

This study was financially supported by Van Lang University, Vietnam.

#### REFERENCES




- [1] X. -B. Luo, R. Hu, S. Liu, and K. Wang, "Heat and fluid flow in high-power LED packaging and applications," *Progress in Energy and Combustion Science*, vol. 56, pp. 1-32, Sep. 2016, doi: 10.1016/j.pecs.2016.05.003.
- [2] Y. Peng *et al.*, "Stable and efficient all-inorganic color converter based on phosphor in tellurite glass for next-generation laser-excited white lighting," *Journal of the European Ceramic Society*, vol. 38, no. 16, pp. 5525-5532, Dec. 2018, doi: 10.1016/J.JEURCERAMSOC.2018.08.014.
- [3] Y. Peng, Q. Sun, L. Jiaxin, and H. Cheng, "Fabrication of stacked color converter for high-power WLEDs with ultra-high color rendering," *Journal of Alloys and Compounds*, vol. 850, p. 156811, Jan. 2021, doi: 10.1016/j.jallcom.2020.156811.
- [4] R. Kobayashi, H. Tamura, Y. Kamada, M. Kakihana, and Y. Matsushima, "A New Host Compound of Aluminum Lithium Fluoride Oxide for Deep Red Phosphors Based on Mn<sup>4+</sup>, Fe<sup>3+</sup>, and Cr<sup>3+</sup>," *ECS Transactions*, vol. 88, no. 1, pp. 225-236, 2018, doi: 10.1149/08801.0225ecst.
- [5] S. Sakurai, T. Nakamura, and S. Adachi, "Synthesis and properties of Rb<sub>2</sub>GeF<sub>6</sub>:Mn<sup>4+</sup> red-emitting phosphors," *Japanese Journal of Applied Physics*, vol. 57, no. 2, p. 022601, 2018, doi: 10.7567/JJAP.57.022601.
- [6] Y. Wen, Z. Li, D. Chen, and S. Man, "Preparation and Optical Properties of Cr<sup>3+</sup> Doped CaAlBO<sub>4</sub> Red Phosphor," in *IOP Conference Series: Earth and Environmental Science*, vol. 714, no. 3, p. 032087, 2021, doi: 10.1088/1755-1315/714/3/032087.
- [7] T. Jansen *et al.*, "Narrow Band Deep Red Photoluminescence of Y<sub>2</sub>Mg<sub>3</sub>Ge<sub>3</sub>O<sub>12</sub>:Mn<sup>4+</sup>,Li<sup>+</sup> Inverse Garnet for High Power Phosphor Converted LEDs," *ECS Journal of Solid State Science and Technology*, vol. 7, no. 1, p. R3086, 2018, doi: 10.1149/2.0121801jss.
- [8] S. I. Yamamoto, K. Ohyama, T. Ban, and T. Nonaka, "Crystal structure dependence of red to green light emission by LaOF : Yb<sup>3+</sup>/Er<sup>3+</sup> up-conversion phosphor," *Materials Research Express*, vol. 6, no. 3, p. 036202, 2019, doi: 10.1088/2053-1591/aaf35a.
- [9] Z. Abbas *et al.*, "A systematic study on optoelectronic properties of Mn<sup>4+</sup>-activated Zr-based hexafluoride red phosphors X<sub>2</sub>ZrF<sub>6</sub> (X = K, Na, Cs): first-principles investigation and prospects for warm-white LEDs applications," *Physica Scripta*, vol. 96, no. 1, p. 015801, 2021, doi: 10.1088/1402-4896/abc646.
- [10] X. L. Dou, X. Y. Kuang, X. X. Xia, and M. Ju, "Exploration of the structural and optical properties of a red-emitting phosphor K<sub>2</sub>TiF<sub>6</sub>:Mn<sup>4+</sup>," *Chinese Physics B*, vol. 28, no. 1, pp. 017107, 2019, doi: 10.1088/1674-1056/28/1/017107.
- [11] L. A. Diaz-Torres *et al.*, "Long-lasting green, yellow, and red phosphorescence of carbon dots embedded on ZnAl<sub>2</sub>O<sub>4</sub> nanoparticles synthesized by a combustion method," *Journal of Physics D: Applied Physics*, vol. 51, no. 41, p. 415104, 2018, doi: 10.1088/1361-6463/aadbda.
- [12] J. Sun *et al.*, "Three Times Lifetime Improvement of Red-Emitting Organic Light-Emitting Diodes Based on Bipolar Host Material," *ECS Journal of Solid State Science and Technology*, vol. 7, no. 5, p. R57, 2018, doi: 10.1149/2.0281805jss.
- [13] R. Liu and X. Wang, "Luminescent properties of a novel green phosphor CePO<sub>4</sub>-6LaPO<sub>4</sub>:Tb<sup>3+</sup>," *IOP Conference Series: Earth and Environmental Science*, vol. 267, no. 3, p. 032101, May 2019, doi: 10.1088/1755-1315/267/3/032101.
- [14] Q. Y. Zheng, Y. Li, W. J. Wu, M. M. Shi, B. B. Yang, and J. Zou, "Effect of sintering temperature on luminescence properties of borosilicate matrix blue-green emitting color conversion glass ceramics," *Chinese Physics B*, vol. 28, no. 10, p. 108102, 2019, doi: 10.1088/1674-1056/ab3f97.
- [15] S. Hariyani, E. Armijo, and J. Brgoch, "Broad Green Emission in the Leucite-Like Cs<sub>2</sub>ZnSi<sub>3</sub>O<sub>12</sub>:Eu<sup>2+</sup> Phosphor," *ECS Journal of Solid State Science and Technology*, vol. 9, no. 1, p. 016015, 2020, doi: 10.1149/2.0222001JSS.
- [16] S. Kumar, S. Rajawat, R. Purohit, and M. M. Malik, "Optical properties of BCNO nano phosphor synthesized using novel green technology," *Materials Research Express*, vol. 6, no. 10, p. 105027, 2019, doi: 10.1088/2053-1591/ab3741.
- [17] S. E. Elhadi, Y. Lu, and C. Liu, "Blue and green emission from Ho<sup>3+</sup> doped zinc titanate phosphor thin films by sol-gel," *Materials Research Express*, vol. 7, no. 1, p. 016402, 2020, doi: 10.1088/2053-1591/ab589e.






- [18] D. S. Bobade, and P. B. Undre, "Green Synthesis of  $\text{Ce}^{3+}$  Doped  $\text{ZnAl}_2\text{O}_4$  Phosphor Using Aloe -Vera Extract and Its Characterization," *Journal of Physics: Conference Series*, vol. 1644, no. 1, p. 012032, Oct. 2020, doi: 10.1088/1742-6596/1644/1/012032.
- [19] Q. Y. Wang *et al.*, "Photoluminescence Spectra Changes and Thermal Stability Improvement for  $\text{Ba}_{1.98}\text{Mg}_{1-x}\text{Al}_2\text{Si}_{2-x}\text{O}_7:0.02\text{Eu}^{2+}$  Green Phosphor with Al-Al replacing Si-Mg," *ECS Journal of Solid State Science and Technology*, vol. 10, no. 3, p. 036004, Mar. 2021, doi: 10.1149/2162-8777/abea60/meta.
- [20] F. C. Lu, L. J. Bai, Z. P. Yang, and J. B. Zhou, "Synthesis, Crystal Structure and Photoluminescence of a  $\text{Gd}_5\text{Si}_3\text{O}_{12}\text{N}:\text{Eu}^{2+}$  Green Emitting Phosphor," *ECS Journal of Solid State Science and Technology*, vol. 7, no. 9, p. R131, 2018, doi: 10.1149/2.0141809jss.
- [21] Q. Dong *et al.*, "Small Thermal Quenching, Narrow Green Emitting  $\gamma\text{-AlON}:\text{Ce}^{3+},\text{Mn}^{2+}$  Phosphor: Luminescence and Energy Transfer," *ECS Journal of Solid State Science and Technology*, vol. 7, no. 12, p. R215, 2018, doi: 10.1149/2.0161812jss.
- [22] J. Dutta and V. K. Rai, "Zirconia based  $\text{Ho}^{3+}-\text{Yb}^{3+}$  codoped upconverting nanophosphors for green light emitting devices applications," *Methods and Applications in Fluorescence*, vol. 6, no. 2, p. 025003, 2018, doi: 10.1088/2050-6120/aa89bf.
- [23] Y. Fu *et al.*, "Comparison of superstar  $\text{CsPbBr}_3$  and classical  $\text{LaPO}_4:\text{Tb}^{3+},\text{Ce}^{3+}$  green-emitting nanophosphors," *Materials Research Express*, vol. 6, no. 5, p. 055017, 2019, doi: 10.1088/2053-1591/ab0165.
- [24] W. Zhang, L. Wu, Z. Su, H. S. Yang, and W. Xie, "Low color temperature, high color rendering index candlelight style white organic light-emitting devices with a fac-tris (mesityl-2-phenyl-1H-imidazole) iridium (III) blue emitting layer," *Materials Research Express*, vol. 6, p. 016205, 2019, doi: 10.1088/2053-1591/aaecc0.
- [25] P. S. Dutta and K. M. Liotta, "Full Spectrum White LEDs of Any Color Temperature with Color Rendering Index Higher Than 90 Using a Single Broad-Band Phosphor," *ECS Journal of Solid State Science and Technology*, vol. 7, no. 1, p. R3194, 2018, doi: 10.1149/2.0251801jss.
- [26] J. Yan, W. Zhao, and Y. Su, "LED filament standard lamp for total luminous flux with uniform spatial distribution," in *Journal of Physics: Conference Series*, vol. 1345, no. 3, p. 032046, Nov. 2019, doi: 10.1088/1742-6596/1345/3/032046.
- [27] S. V. Solyonyj, A. V. Rabin, O. Solenaya, and V. P. Kuzmenko, "Definition and approximation of the light flux degradation of a LED lamp," *IOP Conference Series: Materials Science and Engineering*, vol. 734, no. 1, p. 012197, 2020, doi: 10.1088/1757-899X/734/1/012197.
- [28] M. Huriev and P. I. Neyezhmakov, "Method of Reproduction of the Luminous Flux of the LED Light Sources by a Spherical Photometer," *Journal of Physics: Conference Series*, vol. 972, no. 1, p. 012028, Feb. 2018, doi: 10.1088/1742-6596/972/1/012028.

## BIOGRAPHIES OF AUTHORS



**Phung Ton That**    was born in Thua Thien-Hue, Vietnam. He received the B.Sc. degree in electronics and telecommunications engineering (2007) and the M.Sc. degree in electronics engineering (2010) from the University of Technology, Vietnam. He is currently a lecturer at the Faculty of Electronics Technology (FET), Industrial University of Ho Chi Minh City. His research interests are optical materials, wireless communication in 5G, energy harvesting, performance of cognitive radio, physical layer security and NOMA. He can be contacted at email: tonthatphung@iuh.edu.vn.



**Phan Xuan Le**    received a Ph.D. in Mechanical and Electrical Engineering from Kunming University of Science and Technology, Kunming city, Yunnan province, China. Currently, He is a lecturer at the Faculty of Engineering, Van Lang University, Ho Chi Minh City, Viet Nam. His research interests are optoelectronics (LED), power transmission and automation equipment. He can be contacted at email: le.px@vlu.edu.vn.